Geophysical Journal International

Geophys. J. Int. (2012) **189,** 1753–1770 doi: 10.1111/j.1365-246X.2012.05457.x

Delineating complex spatiotemporal distribution of earthquake aftershocks: an improved Source-Scanning Algorithm

Yen-Che Liao,[1] Honn Kao,[2,3] Andreas Rosenberger,[2] Shu-Kun Hsu[1] and Bor-Shouh Huang[4]

[1] *Institute of Geophysics, National Central University, Jhongli, Taiwan. E-mail: yencheliao@gmail.com*
[2] *Geological Survey of Canada, Pacific Geoscience Centre, Sidney, BC, Canada*
[3] *School of Earth and Ocean Sciences, University of Victoria, BC, Canada*
[4] *Institute of Earth Sciences, Academia Sinica, Taipei, Taiwan*

Accepted 2012 March 10. Received 2012 March 9; in original form 2011 February 4

SUMMARY

Conventional earthquake location methods depend critically on the correct identification of seismic phases and their arrival times from seismograms. Accurate phase picking is particularly difficult for aftershocks that occur closely in time and space, mostly because of the ambiguity of correlating the same phase at different stations. In this study, we introduce an improved Source-Scanning Algorithm (ISSA) for the purpose of delineating the complex distribution of aftershocks without time-consuming and labour-intensive phase-picking procedures. The improvements include the application of a ground motion analyser to separate *P* and *S* waves, the automatic adjustment of time windows for 'brightness' calculation based on the scanning resolution and a modified brightness function to combine constraints from multiple phases. Synthetic experiments simulating a challenging scenario are conducted to demonstrate the robustness of the ISSA. The method is applied to a field data set selected from the ocean-bottom-seismograph records of an offshore aftershock sequence southwest of Taiwan. Although visual inspection of the seismograms is ambiguous, our ISSA analysis clearly delineates two events that can best explain the observed waveform pattern.

Key words: Earthquake source observations; Computational seismology; Asia.

1 INTRODUCTION

The study of earthquake aftershocks is one of the cornerstones for earthquake research. Among various topics of interest, one of the most fundamental issues is the precise delineation of the spatiotemporal distribution of aftershock hypocentres. Such information is critical to the identification of rupture geometry, characterization of source processes, as well as the investigation of regional tectonic stress and strain variations.

Conventional ways to locate aftershocks can be generally grouped into two categories. The first one determines the origin time and hypocentre of each aftershock independently (i.e. the 'absolute' approach). The solution is obtained by either minimizing the misfit between the observed arrival times of various seismic phases (e.g. *P* and/or *S*) and the theoretically predicted ones (e.g. Lee & Lahr 1975; Klein 1978; Engdahl 2006), or by maximizing intersection of equal-differential-time surfaces constructed from arrival pairs (e.g. Zhou 1994; Font *et al.* 2004). The alternative approach determines the precise 'relative' positions of a group of events by joint inversion of the hypocentral mislocations and origin time-shifts (e.g. the joint hypocentre determination method, Douglas 1967), or more recently by minimizing the residual between the observed and theoretical traveltime differences (the double-difference algorithm, Waldhauser & Ellsworth 2000). A more detailed review of earthquake location methods is given by Thurber (2011). Despite the tremendous algorithmic advances, a collection of precise arrival time data, either from phase picking or from cross-correlation of selected waveforms (e.g. Du *et al.* 2004), is intrinsically required.

A common feature of aftershock distribution is that they often occur closely in both time and space. Depending on the type of tectonic setting and the size of the main shock, aftershocks can also occur in large numbers. As a result, seismic waveforms of different aftershock events can arrive at the same recording stations with little or no time difference. These entangled waveforms would create a very difficult situation for phase picking, which in turn results in large hypocentre uncertainties and possibly missed events. This problem is particularly severe during the first few hours after a big main shock when the level of aftershock activity is the highest. Furthermore, it might be difficult to maintain a consistent quality if phase picking is performed manually by a group of analysts. Even for an experienced analyst, the task of correctly correlating phases and picking arrivals for an aftershock sequence (or a cluster of earthquakes) would be both time consuming and labour intensive.

To avoid the necessity of phase picking and the ambiguity of associating the same phases at different stations, Kao & Shan (2004) proposed an alternative approach for locating seismic sources. The method, named the Source-Scanning Algorithm (SSA), calculates the 'brightness' function for the entire model domain, including both time and space, from observed waveforms to illuminate the most likely locations of seismic sources. Although the concept of the SSA is ideally suited for locating closely distributed hypocentres, its practice has yet to be successful because of a number of technical concerns. Among them, finding a robust way to reduce or eliminate artefacts because of incorrect association of the same phases at different stations is perhaps the foremost one.

In this paper, we present an improved version of the SSA (ISSA) that incorporates specific modifications to enhance its capability to reliably locate a cluster of seismic sources that occur closely in both time and space, such as the complex spatiotemporal distribution of an aftershock sequence. The improved method is carefully calibrated using field observations of a local earthquake ($M_{\rm L} \sim 4.5$) to ensure the consistency with respect to conventional phase-picking methods. For the purpose of demonstration, we apply the ISSA to a set of observations recorded by an ocean-bottom-seismograph (OBS) array that were deployed shortly after the occurrence of the 2006 December Pingtung earthquake offshore, southwest of Taiwan. The number of aftershocks is difficult to determine from the observed waveforms and phases are not easily associated with confidence. Our ISSA analysis unambiguously identifies two events that can best explain the observed waveform pattern. The results also help to identify and eliminate spurious phases unrelated to the aftershock events. Finally, we discuss some practical issues of the ISSA, including its similarity and difference with respect to the more general time-reversal (TR) methods (e.g. Fink 1997; Larmat *et al.* 2006, 2008, 2010), and the possible role of the ISSA in complementing conventional relocation methods to obtain highly accurate hypocentral locations of earthquake and aftershock clusters.

2 METHODOLOGY

The SSA was originally designed to locate non-volcanic tremors with emergent arrivals (Kao & Shan 2004). Recent development of the SSA has expanded its application to other seismological problems such as the rapid identification of fault planes for earthquakes (Kao & Shan 2007; Kao *et al.* 2008), delineation of source characteristics of earthquake doublets (Kan *et al.* 2010) and near-real-time epicentral determination of landslides (Kao *et al.* 2012).

Essentially, the SSA is a systematic grid-search method that determines the optimal distribution of seismic sources based on the recorded waveforms. By assuming a source's origin time (τ) and hypocentral location (η), the definition of its brightness function is

$$\mathrm{br}(\eta, \tau) = \frac{1}{N}\sum_{n=1}^{N} \left|u_n(\tau + t_{\eta,n})\right|, \tag{1}$$

where N is the number of recording stations, u_n is the normalized seismogram (waveform envelope or absolute amplitude) recorded at station n, $t_{\eta,n}$ is the predicted traveltime of a given seismic phase from the assumed source location η to station n. If the assumed τ or η is incorrect, no significant waveform amplitudes can be observed at the corresponding arrival times ($\tau + t_{\eta,n}$) and therefore the brightness value is small. On the other hand, the brightness function is large if the assumed origin time and hypocentre are consistent with the arrival of strong amplitudes at most stations. By systematically scanning through all possible combinations of τ and η, the distribution of brightness can be obtained and seismic sources are illuminated as the brightest spots.

In practice, however, there are always time differences between prediction and observation because of the imperfect velocity model. To incorporate the time differences, the surrounding points of the predicted arrival time in the seismogram are included into the brightness calculation and then eq. (1) is modified as

$$\mathrm{br}(\eta, \tau) = \frac{1}{N}\sum_{n=1}^{N} \left\{ \frac{\sum_{m=-M}^{M} W_m \left|u_n(\tau + t_{\eta,n} + m\delta t)\right|}{\sum_{m=-M}^{M} W_m} \right\}, \tag{2}$$

where M is the number of points within the time window on each side of the predicted arrival time, δt is the sampling time interval. W_m is the weighting factor for the sample m and has the value between 0 and 1 depending on the deviation from the predicted arrival time.

Because the choice of M is not obvious and its effect on the calculated brightness has not been well illustrated, the first improvement we made to the original version of SSA is to specifically link the choice of M to the grid size (Δl) and time step (Δt) used in the scanning process, as

$$M_n^{\rm bf} = \frac{\min\{t_{\eta \pm 0.5\Delta l,n} - t_{\eta,n}\} - 0.5\Delta t}{\delta t} \tag{3}$$

and

$$M_n^{\rm af} = \frac{\max\{t_{\eta \pm 0.5\Delta l,n} - t_{\eta,n}\} + 0.5\Delta t}{\delta t}. \tag{4}$$

Here, $M_n{}^{\rm bf}$ and $M_n{}^{\rm af}$ correspond to the numbers of samples before and after the predicted arrival time at station n, respectively, to be included in the brightness calculation. The term $t_{\eta \pm 0.5\Delta l,n}$ corresponds to the traveltimes from the station n to locations deviated from η by one half of the grid size. Effectively, $M_n{}^{\rm bf}$ and $M_n{}^{\rm af}$ correspond to the shortest and longest possible traveltimes from a source located within a time and space volume as specified by the scanning resolution. In other words, for a given scanning resolution (Δl and Δt), the sum of $M_n{}^{\rm bf}$ and $M_n{}^{\rm af}$ sets the length of the calculation time window that should be approximately one half of the duration of the expected signals. Alternatively, we can deduce the optimal combination of Δl and Δt from the expected signal duration using eqs (3) and (4).

The second improvement was to modify how the weighting factor is assigned to reflect the varying signal-to-noise ratios (S/N) of waveforms from one station to another. This is done by changing W_m in eq. (2) to

$$Wm = W_n^{S*} W_m^{D}, \tag{5}$$

where $W_n{}^S$ is the weighting factor of station n that varies from 1 to 3 depending on the overall waveform S/N (1 for S/N < 2, 2 for S/N between 2 and 10 and 3 for S/N >10), and $W_m{}^D$ is the weighting factor for sample m that deviates from the predicted arrival time by $m^*\delta t$ (i.e. the original W_m in eq. 2). Depending on how confident we are regarding the velocity model used in the traveltime calculation, $W_m{}^D$ can be a Gaussian or cosine function that gives less weight toward the endpoints.

In theory, the weighting factor for each station, $W_n{}^S$, can also be used to compensate any bias caused by uneven station coverage. This is particularly useful if the station density varies dramatically across the scanned region. There can be many different ways to implement such compensation, ranging from a simple adjustment if more than

two stations are located nearby to a more sophisticated scheme that takes account of all factors. In practice, however, the station coverage compensation might not be necessary as long as the station distribution is uniform. Because both the synthetic and observed data sets used in this study have an excellent station distribution, we set W_n^S according to each station's overall waveform S/N only.

In the original version of SSA, all the input waveforms are assumed to be the same phase as that used in the calculation of theoretical traveltimes. When a different phase is present in the input waveforms, its arrival times would be inconsistent with the predicted ones and therefore could not be correctly mapped back to the source location. However, the presence of unpredicted phases effectively raises the noise level of the data that, in turn, might somewhat compromise the overall quality of the brightness image (Kao & Shan 2004). Therefore, the third improvement we made was to pre-process the input waveforms to separate the *P* and *S* energies as much as possible. This is done with a real-time ground motion analyser consisting of a recursive singular-value-decomposition matrix that maps the three-component seismic waveform stream from the geographic coordinate system to the principal coordinate system of the particle motion at the resolution of data sampling interval (Rosenberger 2010). By taking the dip angle (θ) of the first eigenvector of the particle motion at each time instance as a proxy for the overall ground motion, we can use the functions of sin (θ) and cos (θ) as the effective identifiers (in the range of 0–1) for motions in the vertical and horizontal directions, respectively. In other words, we effectively split each seismogram into two traces showing primarily *P* and *S* waves by modulating it with sin (θ) and cos (θ), respectively.

Finally, instead of relying on the brightness function of only one phase (*S*) to locate the source, we tried to improve the SSA by including constraints from both *P* and *S* phases. Although theoretically the brightness function should have a better resolution if it combines the contributions from both phases, in reality the possibility of having more artefacts is significantly increased because of the presence of converted/scattering waves that arrive after the *P* phase. A practical way to minimize the artefacts resulting from unaccounted phases is to redefine the final brightness function as

$$\mathrm{br}\,(\eta,\,\tau) = \sqrt{\mathrm{br}\,(\eta,\,\tau)_p^2 * \mathrm{br}\,(\eta,\,\tau)_s^2}, \tag{6}$$

where $\mathrm{br}(\eta,\,\tau)_p$ and $\mathrm{br}(\eta,\,\tau)_s$ correspond to the brightness functions calculated from the split waveforms containing primarily the *P* and the *S* energies, respectively. This revised formula ensures that the seismic source is illuminated as a bright spot only when both *P* and *S* brightness functions are significant.

3 SYNTHETIC EXPERIMENTS

We design a series of synthetic experiments that mimic an extremely complex scenario of aftershocks to demonstrate the advantages of the ISSA over traditional earthquake location methods. Specifically, we challenge the difficult situation in which most methods are expected to fail, that is several aftershocks occurring almost simultaneously at various segments of the fault such that the first arrivals observed at different stations correspond to different events.

Fig. 1 shows the configuration of the experiment. The model covers a volume of 200 km (*x*-direction) by 200 km (*y*-direction) by 70 km (*z*-direction). A small array of eight stations (ST01–ST08) is placed in the region with a station spacing of at least 50 km. The main shock is assumed to have ruptured a 90-km vertical fault over a depth range of 20 km in the direction of NNW–SSE, which is a likely scenario for an event with $M_w \geq 7.5$. Three consecutive aftershock events (S01, S02 and S03) are placed 2 s apart (origin times at 10, 12 and 14 s, respectively) at the starting, middle and ending points of the fault. To make the case even more complicated, their focal depths are also set to be different (Fig. 1a).

All three events are assumed to have the same dip-slip focal mechanism, a triangle source time function of 0.5 s, and the same amount of seismic moment. We generate the synthetic seismograms for each source using the frequency-wavenumber integration method of Zhu & Rivera (2002) and a simplified 1-D layered velocity model derived from an OBS refraction study in the offshore region southwest of Taiwan (McIntosh *et al.* 2005). The synthetic waveforms of all three events are then merged together according to their respective arrival times at individual stations. As the traveltime is a function of the relative position between the source and the station, this means that the order of arrival for the same phase may not necessarily follow the order of event occurrence (Fig. 1b). In other words, it is not obvious from the composite waveforms to decide how many consecutive events might exist, and the location determined from the timing of first arrivals would be erroneous.

We use an efficient finite-difference algorithm developed by Hole & Zelt (1995) to calculate the traveltimes of *P* and *S* phases from each station to all gridpoints and store the results online for fast retrieval. The first step in our data processing is the separation of *P* and *S* energies for each set of three-component synthetic seismograms using the real-time ground motion analyser (Fig. 1c). Then, the waveform envelope of the *P* energy trace split from the vertical component (i.e. the Z_p component, Fig. 1c) is used to calculate the *P* brightness function, that is $\mathrm{br}(\eta,\,\tau)_p$ in eq. 6. The *S* brightness function is derived from the amplitude envelope of the maximum horizontal motion by combining the two horizontal components containing the *S* energy (i.e. *Ns* and *Es*, Fig. 1c). To prevent bias because of amplitude attenuation with epicentral distance, each envelope is individually normalized against its largest amplitude before the corresponding brightness function is calculated. The scanning is performed at a time step of 0.2 s (Δt in eqs 3 and 4) with a grid size of 1 km (Δl) in all directions. For seismograms sampled at 40 points per second, such a scheme corresponds to M_n^{bf} and M_n^{af} being 6 for the *P* phase scanning (i.e. the length of each time segment used in the brightness calculation is ∼0.3 s) and 8 for the *S* phase scanning (i.e. a time segment of ∼0.4 s), respectively.

Fig. 2(a) shows the results of applying the proposed ISSA to the synthetic data set. To facilitate the discussion of results from different experiments, we normalize the brightness function between 0 and 1 with respect to the maximum value. As shown at the bottom panel of Fig. 2(a), three clear peaks with $\mathrm{br}(\eta,\,\tau)$ values of 1.0, 0.95 and 0.73 can be identified at 10, 12 and 14 s, respectively, corresponding exactly to the origin times of the input events. In comparison, the $\mathrm{br}(\eta,\,\tau)$ value is significantly less than 0.4 once the scanning moves away from the origin times of the input events. To demonstrate how the brightness image illuminates the three seismic sources, we use a threshold of 0.5 and plot the composite brightness distribution for the entire scanned time period (i.e. from 0 to 20 s) in both map view and cross-section (middle and top panels, Fig. 2a). The locations corresponding to the three peaks in the brightness function are marked by green circles, and they perfectly match the input source distribution (Fig. 1a).

There are some minor spots scattering in the vicinity of the true source locations, mainly as a result of the interferences of phases from different sources. Consequently, we can follow the practice of Kao & Shan (2004) and use the 85 per cent contour of the largest peak brightness to estimate the corresponding uncertainties

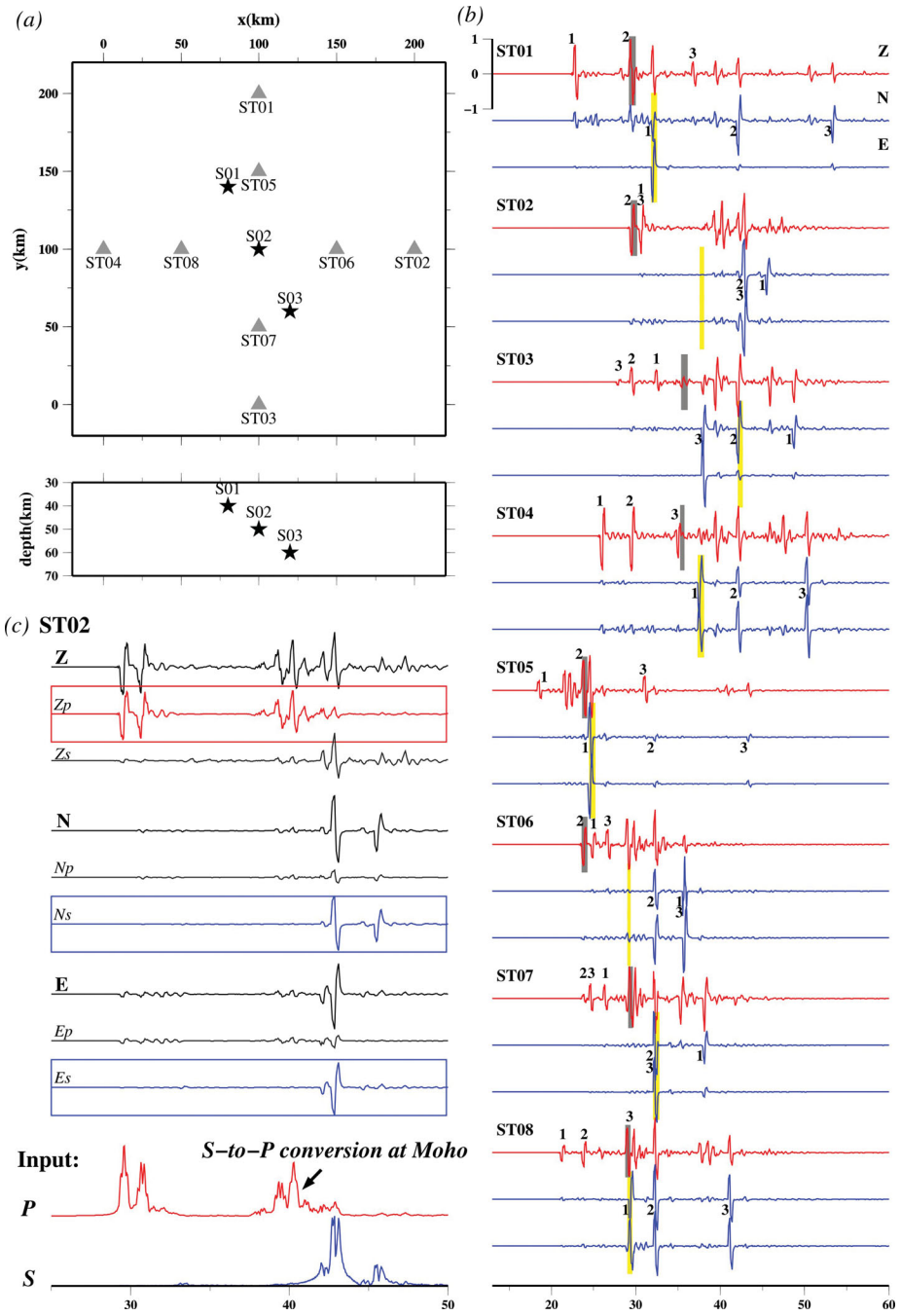

Figure 1. Configuration and waveforms of synthetic events for our experiments. (a) Map and cross-section showing the hypocentres of the three hypothetical aftershock events (stars) and eight seismic stations (triangles). (b) Three-component synthetic seismograms (Z-component in red; N- and E-components in blue) with the numbers (1, 2 and 3) marking the corresponding *P* and *S* arrivals of the three events. The grey and yellow bars mark the predicted arrivals from erroneous solutions when only *P* or *S* phases are used in the source-scanning process, as discussed in the text. (c) An example illustration of the procedures for data processing. Each waveform (Z-, N-, or E-component) is split into two traces containing the *P* (*Zp*, *Np* and *Ep*) and the *S* (*Zs*, *Ns* and *Es*) energies. The *P*-wave envelope is constructed from the *Zp* trace (red box); whereas the *S*-wave envelope is derived from combining the *Ns* and *Es* traces (blue boxes). These envelopes are input for the source-scanning analysis.

of our ISSA solutions. Based on the brightness images shown in Fig. 2(a), the horizontal and vertical uncertainties are ±2 km and ±5 km, respectively. In other words, the depth uncertainty is about two to three times larger than the horizontal one. This implies that the brightness function is more sensitive to variations in epicentral distance than that in depth.

For comparison, we conduct the following experiments using the same data set but with different location methods to demonstrate the effectiveness and advantages of the proposed ISSA. The first is the traditional approach that estimates the hypocentre and origin time of a seismic source from the timing of first arrivals observed at an array of stations (e.g. the HYPO71 program, Lee & Lahr 1975). We measure the first arrival times from the synthetic seismograms shown in Fig. 1(b) and use them as input to invert for the origin time and location of the source. An obvious drawback of this approach is that it has no ability to resolve all three solutions because only

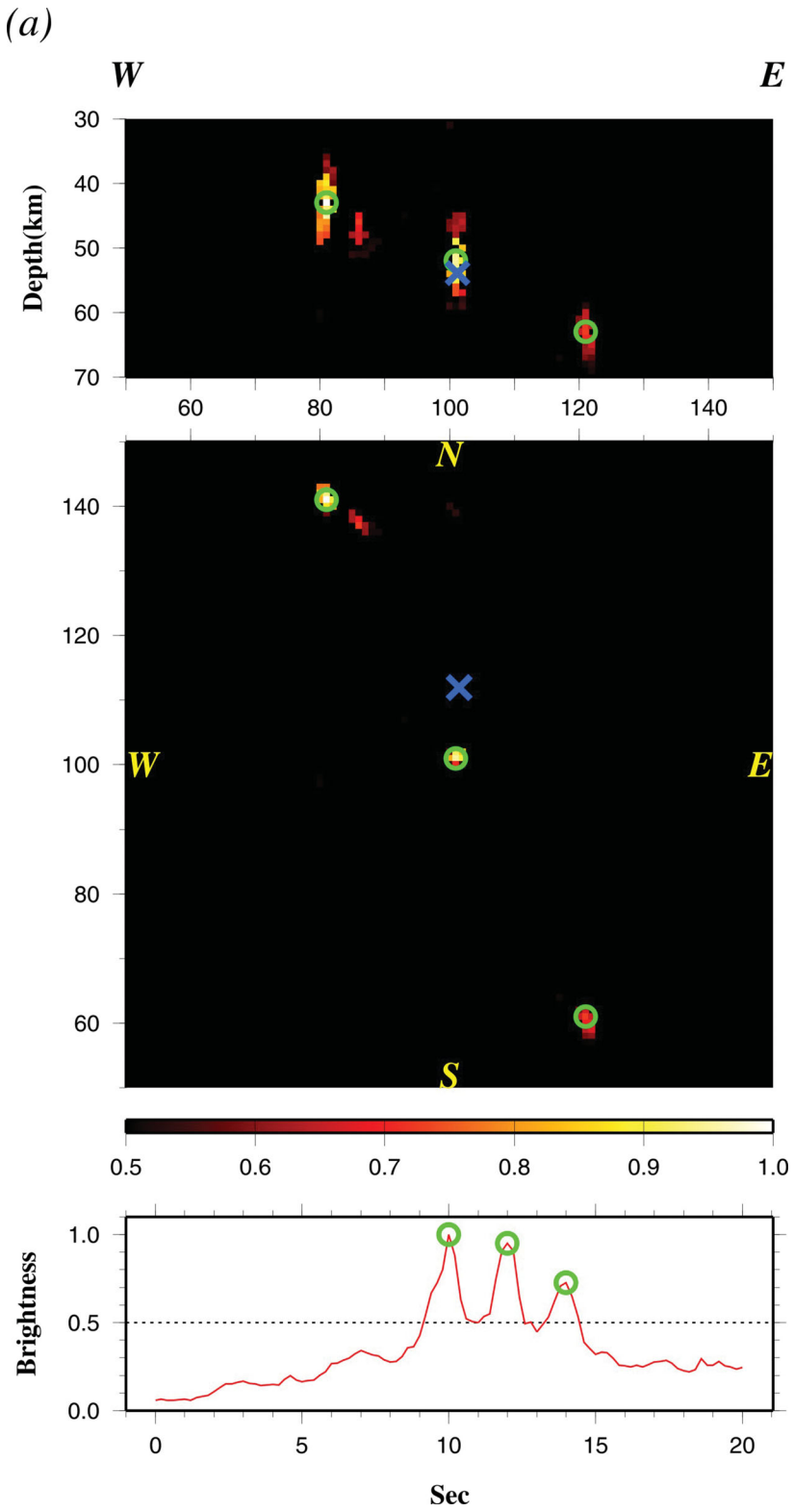

Figure 2. Results of our experiments with synthetic events. (a) Using both *P* and *S* phases in the scanning process (as in the ISSA method proposed in this study). The top and middle panels display the distribution of brightness in E–W cross-section and map view, respectively. The maximum brightness as a function of time is shown at the bottom. The corresponding locations of the three peaks are marked as green circles and coincide exactly to the input sources. In contrast, the solution derived from the timing of first arrivals (blue cross) is an artefact because of the complex source distribution. (b) Similar to (a) but using only the *P*-wave envelopes in the scanning process. Only one event is correctly recovered (green circle), whereas erroneous combination of *P* phases from different events result in many artefacts. One representative example is marked by the grey circle and its predicted time windows of *P* arrivals are marked by grey bars in Fig. 1(b). (c) Similar to (a) but using only the *S*-wave envelopes. Two of the three input sources are correctly recovered (green circles). Predicted time windows of *S* arrivals from one of the artefacts (grey circle) are marked by yellow bars in Fig. 1(b), pin-pointing the origin of brightness contamination.

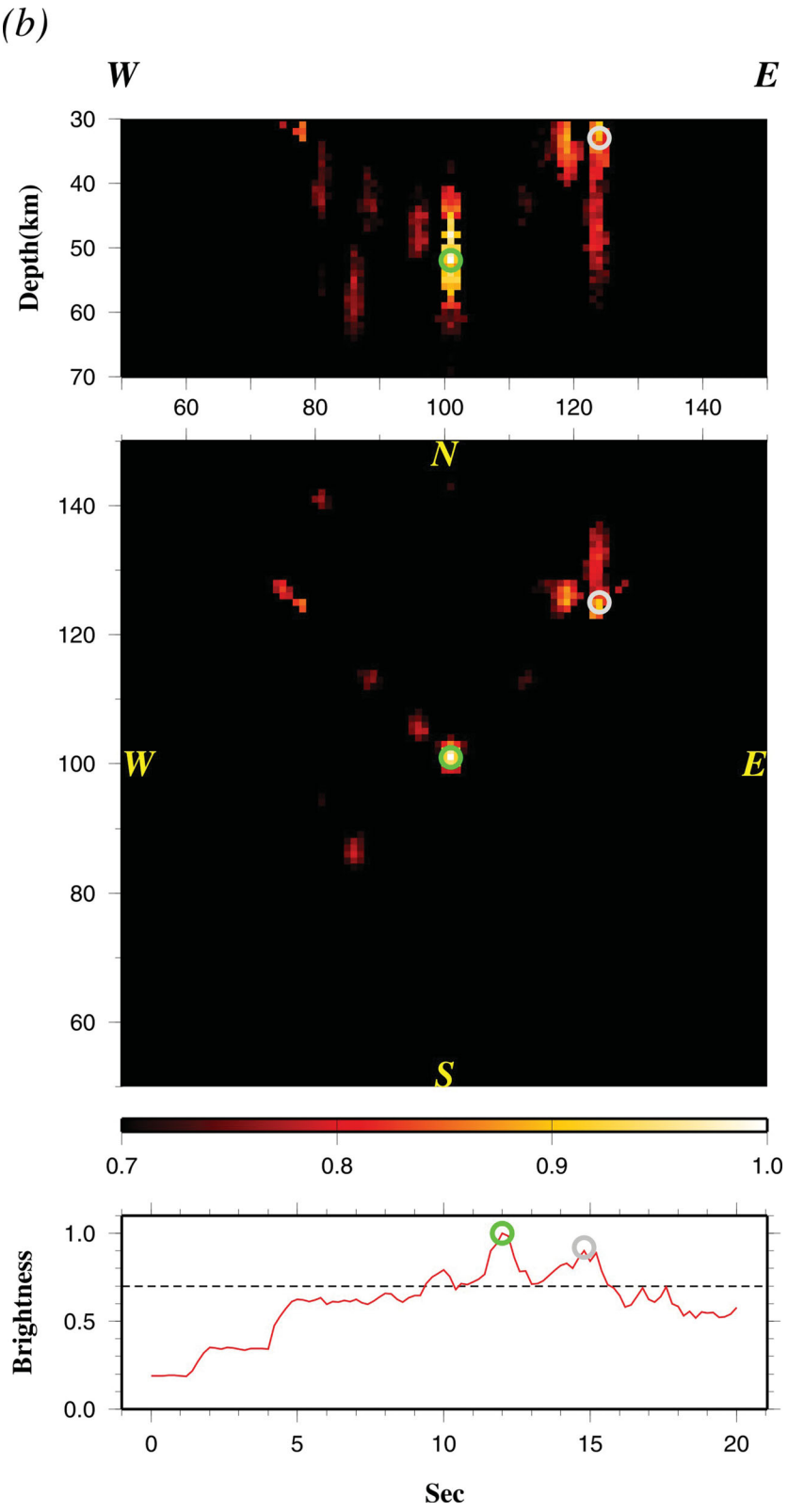

Figure 2. (*Continued.*)

one set of arrival times can be obtained. Moreover, because these first arrivals actually correspond to different sources depending on the relative source-station positions (fourof eight are from the first event, three from the second event and one from the third event; Fig. 1b), the result would be expected to be incorrect with respect to any of the assumed sources. Indeed, the final result indicates a source at 7.79 s with a very large root mean square (rms) error of 1.33 s. This is 2.21 s earlier than the origin time of the first

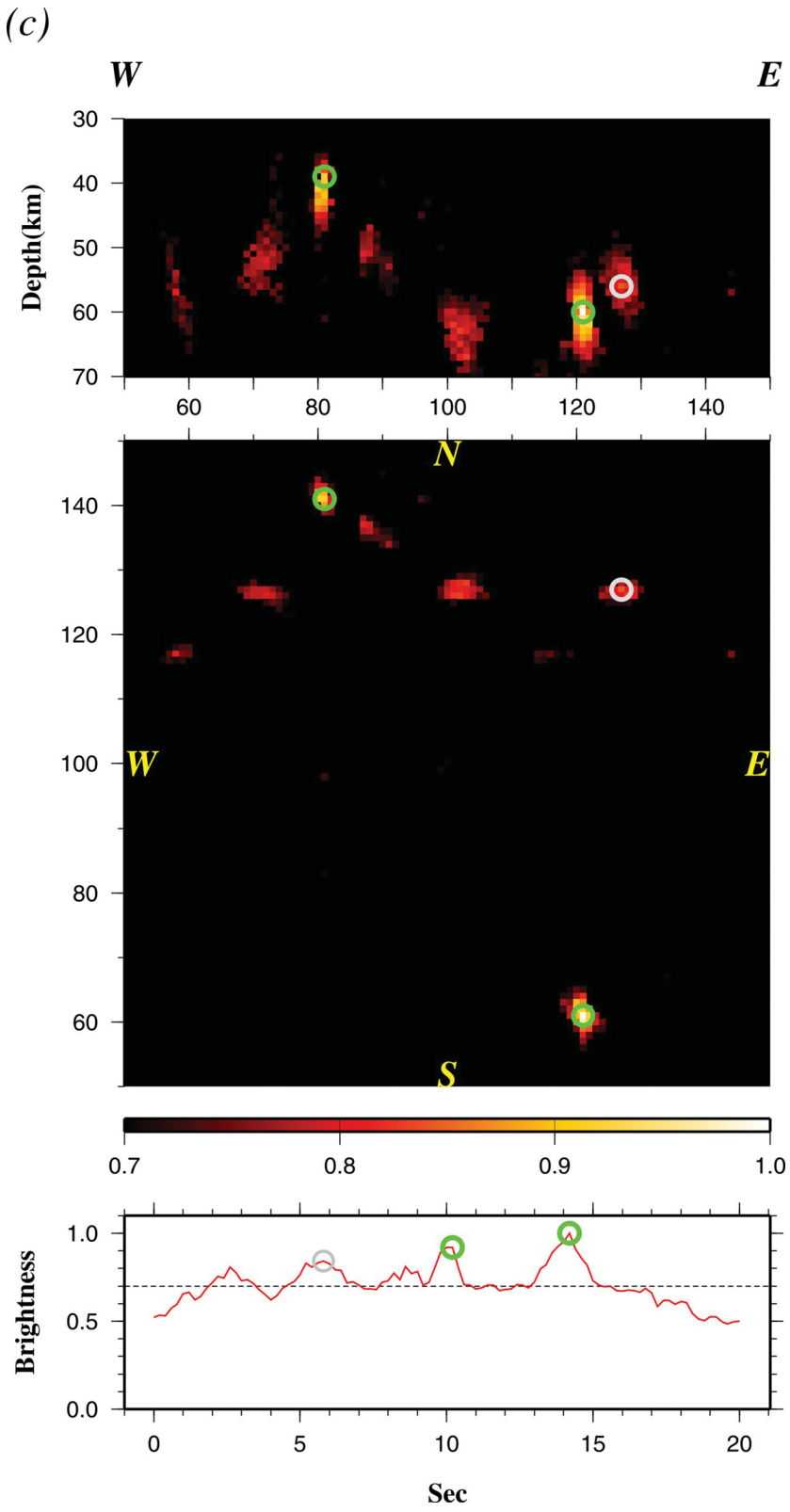

Figure 2. (*Continued.*)

event. The corresponding hypocentre, marked as the blue crosses in Fig. 2(a), is located at 101.3 km (*x*-direction) and 111.7 km (*y*-direction) with a depth of 54 km. The location uncertainty (i.e. one standard deviation) is estimated to be 12 km horizontally and 31 km vertically. We have repeated this experiment using other phase-picking-based methods (e.g. Klein 1978; Zhou 1994; Font *et al.* 2004; Engdahl 2006), and the results are all very similar. The relatively large uncertainties, earlier origin time and mislocated hypocentre all point to the limitation of conventional phase-picking-based methods in this complex situation.

The second and third experiments are similar to our ISSA approach but the scanning was done by the original version of SSA using only one phase. Specifically in the second experiment, the brightness function is derived from waveform envelopes of the vertical component with the theoretical traveltimes calculated from a *P* velocity model. The third scans the horizontal components based on an *S* velocity model. The results of these two experiments are presented in Figs 2(b) and (c), respectively.

The first notable difference in the scanned results, comparing to those produced in the ISSA trial, is the overall higher background noise of the brightness functions (bottom panels, Figs 2b and c). As a result, the brightness peaks become much less apparent with a significantly smaller amplitude contrast with respect to neighbouring times. Although the amplitude contrast is >0.5 for the ISSA result (Fig. 2a), it drops by $\sim$40 per cent to 0.3 if only *P* or only *S* phases are used in the scanning process. To better illuminate the bright spots from the SSA images, we set the plotting scale according to the peak amplitude contrast such that only the brightness values larger than the preset threshold (dashed lines in the lower panels of Fig. 2) are displayed.

For the SSA result derived from *P* energy only (Fig. 2b), we obtain three major brightness peaks above the preset threshold of 0.7 at 10, 12 and 14.6 s. The timing of these peaks appears to be consistent with the input events; however, only the second peak (at 12 s) correctly recovered the corresponding hypocentre (green circles, Fig. 2b). The first peak has a brightness value only slightly above the threshold, whereas the derived hypocentre of the third deviates from the true location by as much as 65 km (Figs 2a and b).

To investigate the possible causes of artefacts in Fig. 2(b), we conduct a forward modelling for the third peak (grey circles, Fig. 2b) and mark the predicted *P* arrivals from the derived solution as grey bars on the Z component seismograms in Fig. 1(b). It turns out that this artefact is constrained jointly by the *P* phase of the second event (e.g. at ST01, ST02, ST05 and ST06), the *P* phase of the third event (e.g. at ST04 and ST08) and other secondary converted phases (e.g. at ST03 and ST07). In other words, the incorrect combination of *P* and converted phases from different events is the primary source of artefacts on the brightness images. This example further demonstrates the importance of introducing additional constraints from both *P* and *S* phases when a complex spatiotemporal distribution of seismic sources is expected.

In contrast, the SSA analysis of using only the *S* energy successfully recovered two events at 10 and 14 s (green circles, Fig. 2c). Although this performance is better than using *P* phases alone, it is still incapable of resolving all sources in a complex situation. One of the biggest issues is the existence of several small peaks above the preset threshold before the assumed first event at 10 s (e.g. 3.5, 5.8 and 8.8 s; lower panel, Fig. 2c). Taking the largest artefact at 5.8 s, for example (grey circles, Fig. 2c), the derived hypocentre is about 40 km from the true location of event 1, 50 km from event 2 and as much as 70 km from event 3 (*cf*. Figs 2a and c). Similarly, we conduct forward modelling for this solution to investigate possible reasons. The calculated *S* arrivals from this erroneous bright spot are marked by yellow bars on the two horizontal-component seismograms in Fig. 1(b). Once again, the accidental combination of the *S* phases from different sources (event 1 for ST01, ST04, ST05 and ST08; event 2 for ST03; event 3 for ST07) and secondary converted phases (e.g. ST02 and ST06) is responsible for the mapped artefact.

We use the same weighting scheme in all the synthetic experiments to ensure a fair comparison among the results. Because the new weighting scheme of ISSA (eq. 5) aims at objectively suppressing the effect of high background noise, it produces no difference in our synthetic experiments as all input waveforms have the same S/N.

On the basis of the above experiments, we conclude that the proposed ISSA with the brightness function constrained by both *P* and *S* phases has a remarkable discriminatory capability compared to previous or traditional seismological methods in delineating the complex spatiotemporal distribution of seismic sources.

4 APPLICATION TO OBS DATA

It is not our intention to promote the ISSA as a total replacement for traditional locating methods when the spatiotemporal distribution of seismic events can otherwise be properly resolved. Instead, we focus on more challenging scenarios such as those presented in the previous section in which all other methods fail to recover the true source patterns. Following this line of reasoning, it becomes impractical, and perhaps even unnecessary, to demonstrate that the ISSA would work under ordinary conditions (e.g. good site conditions, high-quality waveforms, redundant station coverage and seismic events well separated in both time and space). In this section, we try to apply the ISSA to a field OBS data set that has none of the aforementioned merits.

In general, the data quality of OBS stations is worse than that of land stations because of relatively weak coupling between the instrument and the sedimentary environment on the seafloor. Depending on the specific types of OBS, some OBS data may also suffer from disorientation if the instrument is severely tilted because of the rugged bathymetry of the landing site.

The data set used in this demonstration comes from a temporary array of eleven OBSs that were deployed offshore, southwest of Taiwan from 2006 December 27 to 2007 January 03 to record the aftershock sequence of the 2006 December 26 , Pingtung earthquake doublet ($M_{\rm w} \sim 7.1$ and 6.9; red stars, Fig. 3a). This data set is inappropriate for manual phase picking, not only because most aftershocks are relatively small ($M_{\rm L} < 3$), but also the number of recorded events is overwhelming. In addition, the possibility of out-of-sequence arrivals as presented in the previous section cannot be ruled out. Complicating matters further, two out of the 11 OBS stations, OB05 and OB07, have anomalous amplitudes on horizontal components, possibly because of local conditions around the landing sites. All of these issues make it a very challenging problem to determine the spatiotemporal distribution of the 2006 Pingtung aftershock sequence from the collected OBS data.

4.1 Consistency between ISSA and conventional phase-picking method

Before we use the ISSA to systematically locate numerous aftershocks in the OBS data set, it is necessary to assess the consistency between an ISSA solution and the solutions determined by other methods. A moderate-sized event ($M_{\rm L} \sim 4.5$) that occurred on 2006 December 28 in the general area of our OBS array is selected for such a purpose. Based on the distribution of first arrival times at inland stations, the hypocentre is located by the Central Weather Bureau of Taiwan at 120.43°E, 21.96°N with a depth of 32.6 km. A more recent tomography study relocates this event to a shallower depth (22.97 km), but the epicentre remains almost unchanged (120.48°E, 21.95°N; yellow star, Fig. 3a; Liao *et al.* 2008).

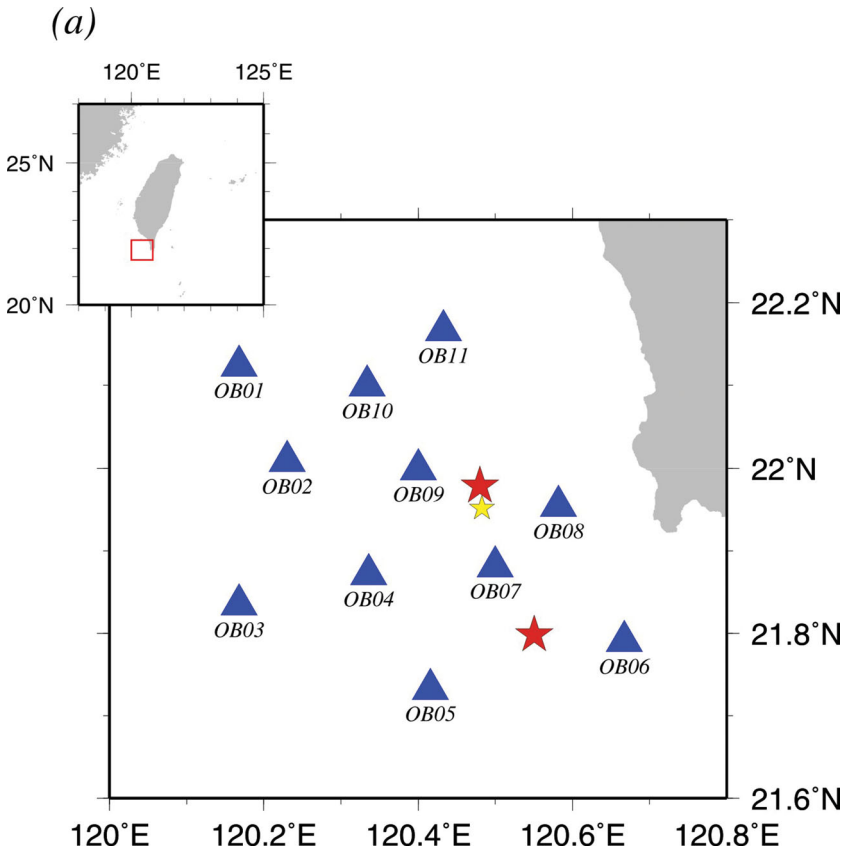

Figure 3. Consistency test between ISSA and the conventional phase-picking method. (a) Map showing the epicentre of a significant aftershock (yellow star) of the 2006 Pingtung, SW Taiwan, the earthquake doublet (epicentres of the twin main shocks are shown as red stars) and the locations of ocean-bottom-seismographs deployed shortly after the main event (blue triangles). (b) Waveform envelopes used in the source-scanning process. *P* and *S* envelopes are plotted in red and blue, respectively. Time windows of *P* and *S* arrivals that correspond to the best ISSA solution are highlighted in light blue and yellow colours, respectively. (c) A snapshot of the brightness distribution for the ISSA solution. The brightest spot is marked by a green circle, which is remarkably consistent with the solution obtained by the conventional phase-picking method (blue circle). Layout is the same as that in Fig. 2.

The dimension of the scanning volume and the data-processing procedures are the same as those described in our synthetic experiments, except that a high-pass filter (>1 Hz) is applied to all seismograms first to remove long-period background noise. The final envelopes of the split *P* and *S* waves, that is the ISSA input, are plotted in red and blue, respectively, in Fig. 3(b). We skip the particle motion analysis for the two stations mentioned earlier (OB05 and OB07) whose horizontal components might have incorrect amplitudes. Their weighting is reduced by 50 per cent in the calculation of brightness functions because the high-passed vertical component is used as the input for both *P* and *S* phases instead of the split waveforms.

We adopt the 3-D *P*-wave velocity model derived from the most recent tomography analysis of the study region (Liao *et al.* 2008) to minimize any possible effect because of the inaccuracy of theoretical traveltimes. Because Liao *et al.* (2008) did not establish the corresponding *S*-wave velocity model; we need to derive it from the *P* velocity model by assuming an appropriate V_p/V_s ratio. Rather than arbitrarily choosing the value of the V_p/V_s ratio, we repeat the scanning process using a broad range of 1.70–2.00 with an increment of 0.01 to obtain the best ISSA solution.

To achieve maximum computing efficiency, the scanning process is conducted in three stages with increasing resolution. Specifically, the first stage scans the entire model space in a grid of 10-km interval with a 10-s time step (i.e. $\Delta l = 10$ km, $\Delta t = 10$ s) to identify the general source location quickly. In the second stage, the scanning is limited to the vicinity of the solutions obtained in the first stage (i.e. ± 20 km and ± 10 s in distance and time) using a finer grid ($\Delta l =$ 2 km) and a smaller time step ($\Delta t = 2$ s). Finally, the grid size is set to 1 km in the third stage to scan the region ± 10 km around the best second-stage solution. We repeat the scanning several times using a Δt ranging from 0.5 to 1.0 s to ensure that the number of samples included in the brightness calculation (eqs 3 and 4) is large enough to tolerate any misalignment between the predicted and observed arrival times. Although such misalignment may be caused by many different factors (e.g. insufficient accuracy of the velocity model, long source time function and poor signal-to-noise ratio), it is best to choose a time step long enough for the predicted time windows to include the peaks in the input envelopes.

The results indicate the highest consistency between the ISSA and the tomography solutions is achieved when the V_p/V_s ratio is set to 1.91 and the scanning interval (Δl) and time step (Δt) for the three stages are 10 km and 10 s, 2 km and 2 s and 1 km and 0.5 s, respectively. The brightness image of the best ISSA solution is shown in Fig. 3(c) and the corresponding predicted arrival time windows for *P* and *S* phases are marked as blue and yellow bars on the input envelopes in Fig. 3(b). The ISSA solution (green circles, Fig. 3c) is practically identical to the relocated solution of tomography (blue circles), demonstrating the remarkable consistency between these two methods when the input data are well behaved.

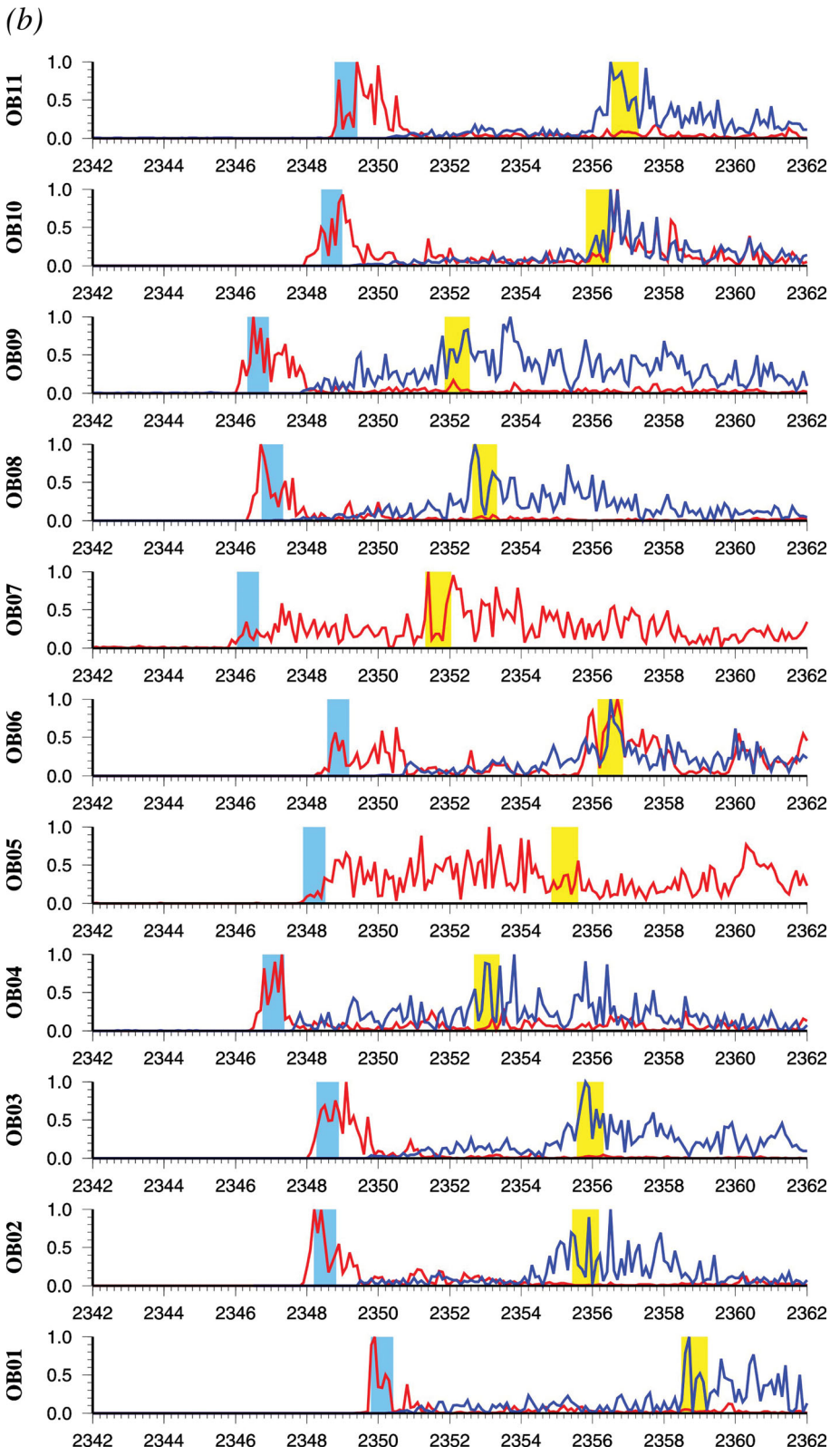

Figure 3. (*Continued.*)

4.2 A complex example

The time window of this complex example is from 6:52:30 to 6:53:20 (i.e. from 3150 to 3200 s after 6 a.m.), 2006 December 28 (UTC). Normalized waveforms of the vertical component are plotted in Fig. 4(a) to demonstrate the difficulty of applying conventional phase-picking methods with confidence. We need not only to pick precisely the arrival times of various seismic phases, but also

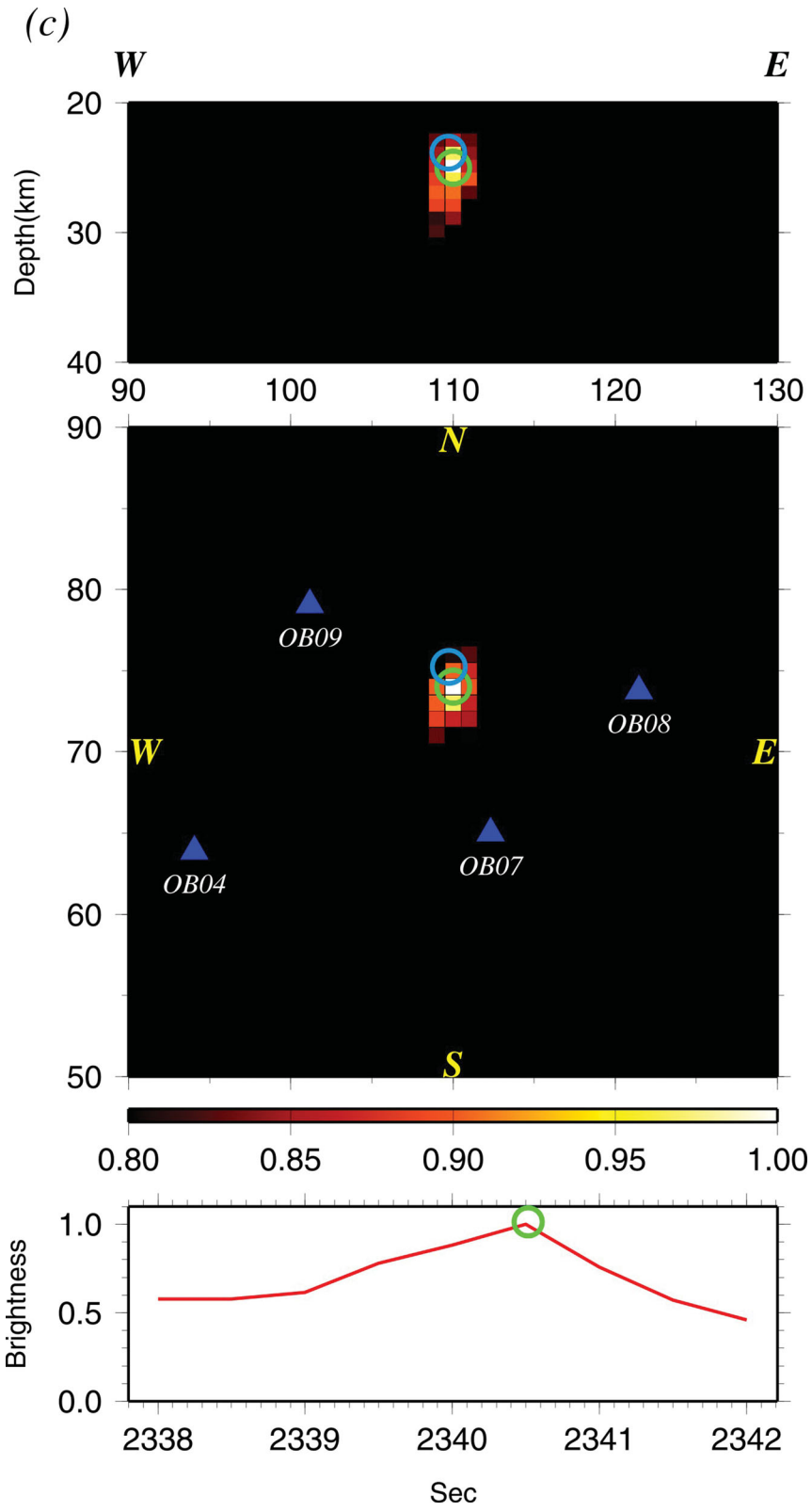

Figure 3. (*Continued.*)

to associate these phases to different events correctly for the entire array. If the waveforms appear to be ambiguous in terms of the number of events, then correctly associating the phases of the same event for all seismograms becomes much more challenging. For examples, the two significant arrivals at 3165 and 3178 s at station OB02 can be interpreted as the typical *P* and *S* phases of a single event. Station OB03 also seems to suggest one single event but with an additional phase in between, possibly refracted or reflected from

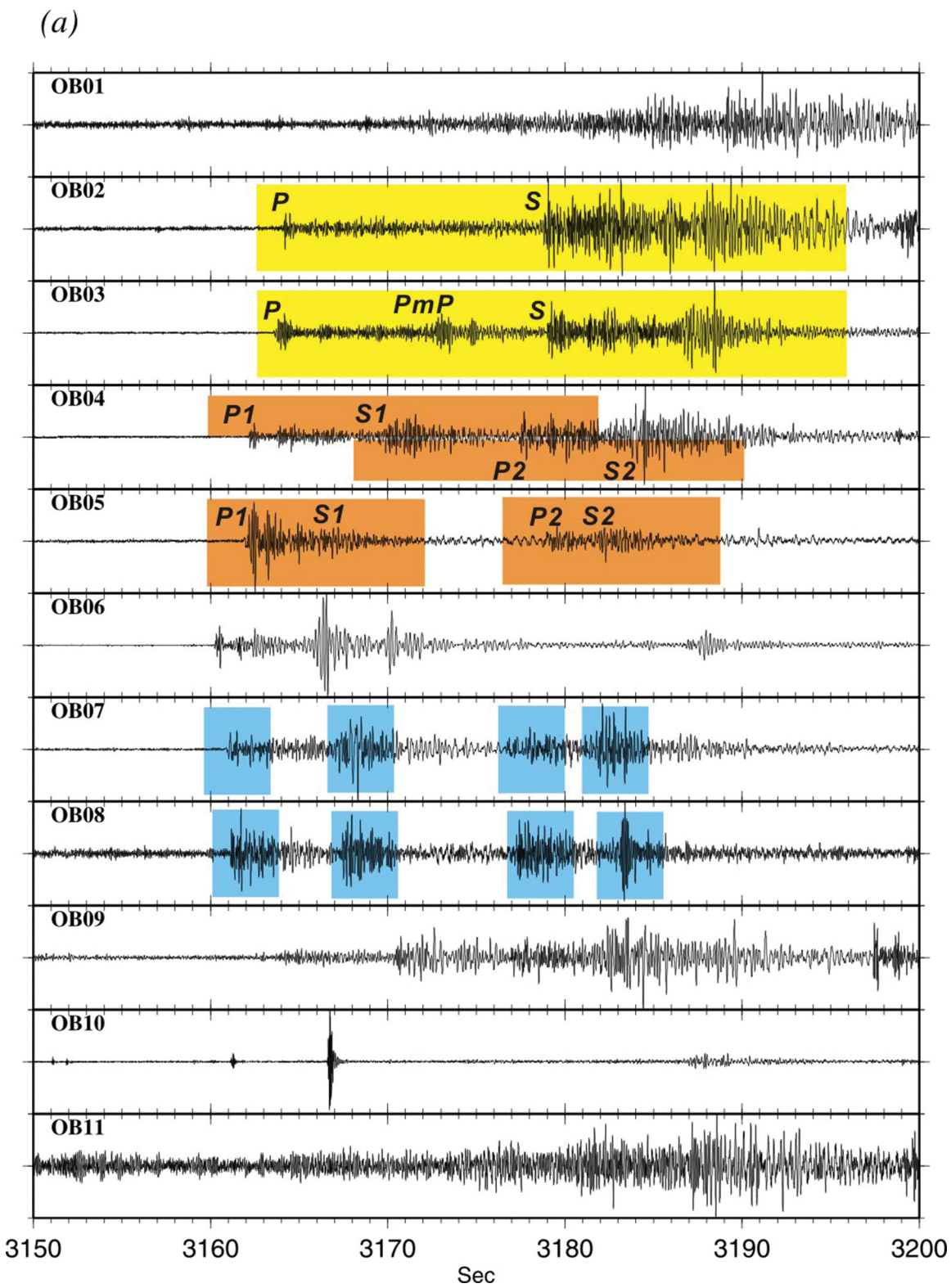

Figure 4. Application of ISSA to an OBS data set selected from the aftershock sequence of the 2006 Pingtung earthquake, SW Taiwan. (a) Z-component seismograms between 6:52:30 to 6:53:20 (i.e. from 3150 to 3200 s after 6 a.m.), 2006 December 28 (UTC). Different colours represent different ways to interpret the observed waveforms. Seismograms from stations OB02 and OB03 suggest the existence of one event with impulsive arrivals of various phases (yellow), whereas OB04 and OB05 seem to be more consistent with two events (light brown). In contrast, OB07 and OB08 imply that four small events might be possible. (b) ISSA analysis results. The brightness function (bottom) shows two clear peaks separated by 17 s with their brightness images plotted in E–W cross-section (top) and on map view (middle). The brightest spots (i.e. corresponding hypocentres) are marked as green and red circles for the first and second events, respectively. (c) Same as (a) but the time windows of *P* and *S* arrivals that correspond to the two ISSA solutions are marked by *P1/S1* (in green) and *P2/S2* (in red), respectively.

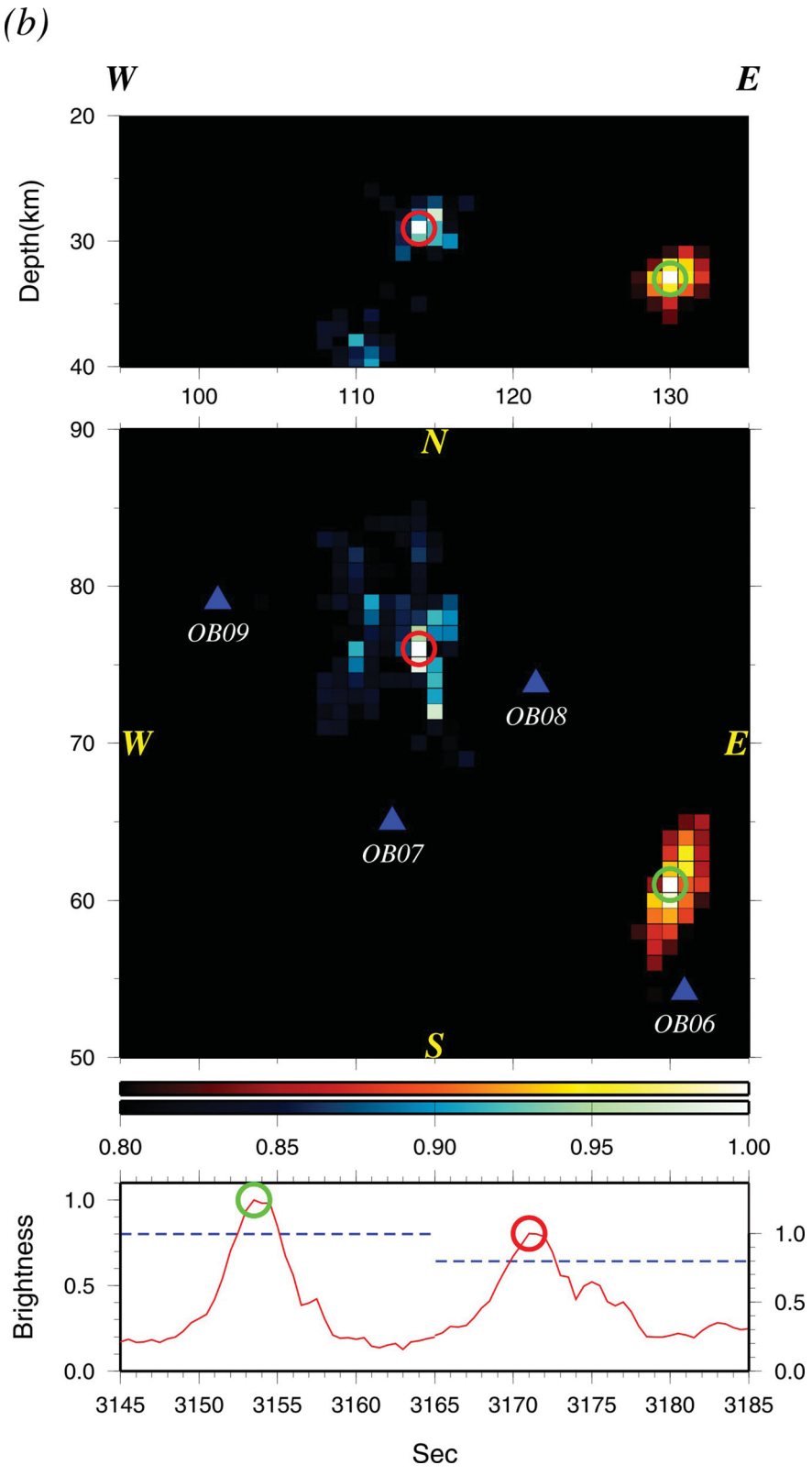

Figure 4. (*Continued.*)

a velocity discontinuity such as the Moho. On the other hand, the waveform of OB04 seems to suggest two events with the phases at 3162 and 3178 s being the *P* and *S* phases of the first event, and those at 3170 and 3184 s belonging to the second event. Perhaps, these two events are completely separated as interpreted on the waveform of OB05 in Fig. 4(a). Moreover, waveforms of OB07 and OB08 appear instead to show four small events. Such a complex waveform pattern makes it difficult to determine exactly

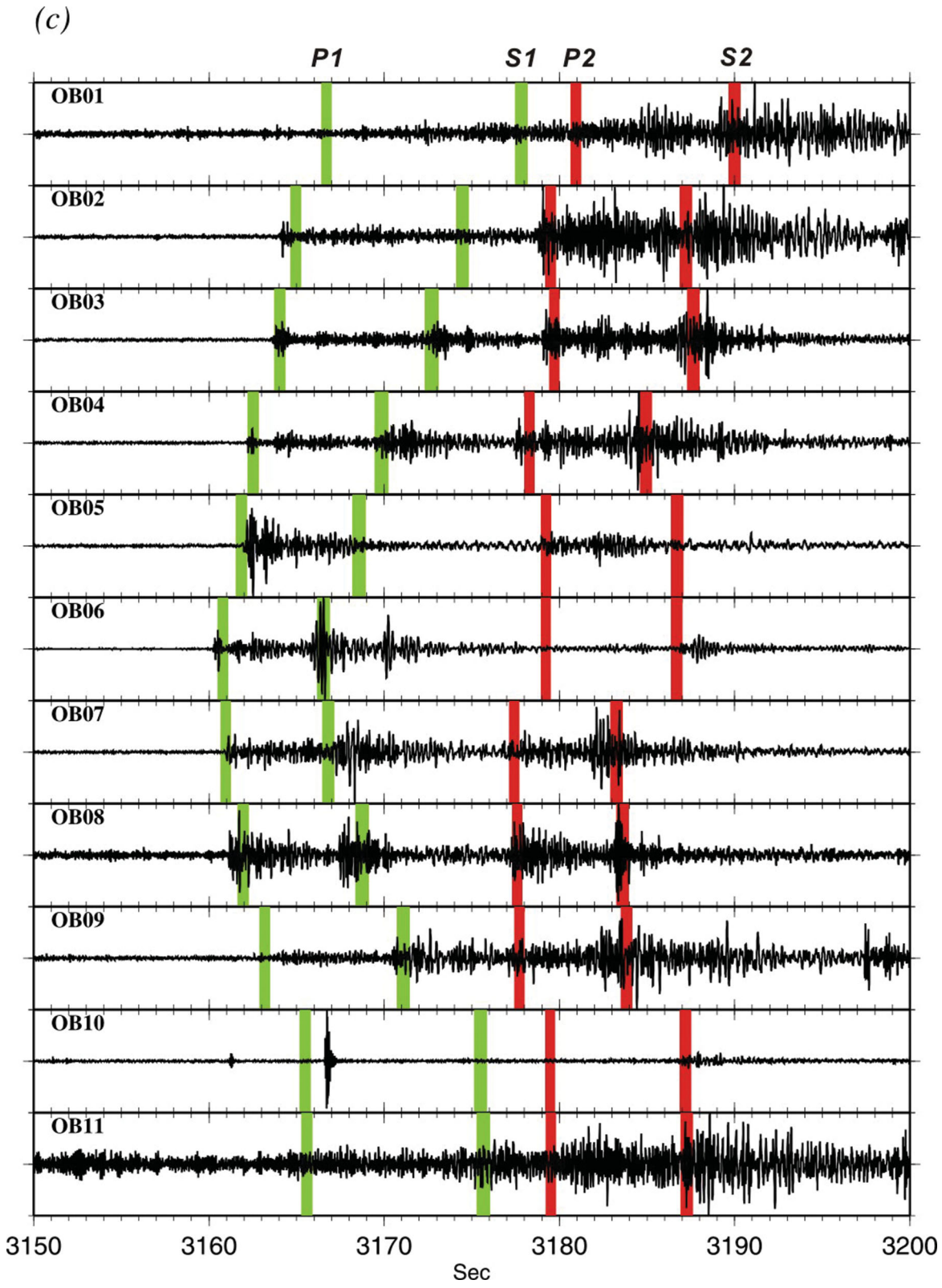

Figure 4. (*Continued.*)

how many events have actually occurred, let alone to pick correctly the different phases for each of the identified events.

We apply the ISSA to this complex case and the results are shown in Fig. 4(b). There are two clear peaks in the brightness function (green and red circles, bottom panel, Fig. 4b), suggesting the existence of two aftershocks separated by a time difference of 17 s. The snapshots of brightness distribution at each peak are shown in both map view (middle panel, Fig. 4b) and cross-section (top

panel) with the brightest spots marked by circles. The horizontal and vertical distances between these two events are about 22 and 4 km, respectively. In Fig. 4(c), we mark the arrivals of the *P* and *S* phases predicted by this two-event model in different colours. Because the ISSA has scanned the entire model space, we have the confidence that this two-event model can best explain the observed waveform pattern. For example, the relatively smaller amplitudes of the first aftershock observed at OB02 and OB03 and the relatively smaller amplitudes of the second event observed at OB06 can all be explained by the relative positions of these stations with respect to the two epicentres (Figs 3a and 4c). For stations OB07 and OB08, the two events appear to show approximately the same amplitudes because the corresponding epicentral distances are about the same. The strong phases at 3161 and 3167 s at OB10 are apparently not associated with either of the identified events, as they are incompatible with all the arrivals observed at other stations. They are mostly likely caused by an unknown small event located very close to the OB10 site.

Generally speaking, the uncertainty of an epicentral location is larger in the vertical direction than in the horizontal direction, as demonstrated in the previous section. For this complex example, however, the brightness images of both aftershocks show the opposite pattern with broader bright areas on the map than in the cross-section (Fig. 4c). The relatively broader bright zones on the horizontal plane probably reflect the increasing possibility of wrongly associating different phases from different stations because of the close proximity of the two aftershocks in both time and space. Nevertheless, none of these scenarios would result in a brightness value larger than the best solution. This further illustrates the merit of the ISSA when we are challenged by a complex distribution of seismic sources.

5 DISCUSSION

The practice of waveform stacking has been very common in seismology to enhance data quality and/or to extract structural information. In this section, we discuss the similarity and differences between the ISSA and other stacking-based methods. We also try to cover some topics related to the performance and application of the ISSA.

5.1 ISSA versus beam-forming and diffraction stacking migration

One of the most common stacking-based methods is the beam forming that determines the back azimuth and incident angle of a wave front propagating across a given seismic array. The beam energy is derived by summing up the time-shifted waveforms according to the theoretical time delays at individual stations (e.g. Ingate *et al.* 1985; Mao & Gubbins 1995). Although the philosophy of utilizing the power of waveform stacking is the same, the ISSA distinguishes itself from the beam-forming method in two major aspects. First, the beam-forming method stacks the entire waveform traces in the beam-energy calculation, whereas the ISSA only sums up waveform amplitudes within specific time windows around multiple phases (in our case, the *P* and *S*). This approach makes it possible to extract additional constraints from the data set without necessarily increasing the number of stations. It also enables the application of ISSA to seismic arrays of different sizes where the full waveform coherence among stations might significantly deteriorate because of the different propagation speeds of *P*, *S* and other phases. Second, the nature of problems targeted by ISSA is fundamentally different from those by the beam-forming method. Although the beam forming is ideal at pinpointing the direction from which the source of energy is coming, it does not actually locate the source. In contrast, the ISSA is designed specifically to illuminate the spatiotemporal distribution of seismic sources within a given model space.

The diffraction stacking migration (DSM, also known as the Kirchhoff migration) is another stacking-based data-processing method that is particularly popular in exploration seismology (e.g. Gray & May 1993; Bevc 1997). The basic principle of DSM is that a point scatter inside the media with a constant wave-propagation speed would create a diffraction hyperbola in the zero-offset seismic section when the recording receivers are closely spaced. Therefore, one can stack the observed amplitudes along the diffraction hyperbola predicted from the assumed wave speed to 'back project' the location of the scatter. Because a seismic reflector can be considered as a dense array of point scatters, the geometry of complex geological structures can be properly identified from the seismic profile after DSM (e.g. Audebert *et al.* 1997).

The SSA/ISSA is conceptually very similar to DSM, except that our target is the spatiotemporal distribution of seismic sources instead of the geometry of structures. Consequently, many differences between the SSA/ISSA and DSM lie in the technical implementation to suit their respective purposes. For example, the waveform amplitudes used in the DSM are taken along the predicted hyperbola in the seismic section (or a somewhat distorted hyperbola depending on the assumed wave speed variation). For most SSA/ISSA applications, however, a seismic section with closely spaced receivers almost never exists. And the corresponding velocity model is always too large and complicated to be represented by a constant wave speed. Therefore, the waveform amplitudes/envelopes used in the brightness calculation cannot be taken from a DSM hyperbola directly. Forward calculation of the theoretical arrival time at each station (from the assumed time and location of a source) is always needed.

Another major difference is the stacking procedure to recover the expected target(s). In a traditional DSM approach, the stacking is performed for each data sample of each seismic trace for the entire seismic section. The final 'migrated' seismic section is a manifestation of the corresponding structures that are independent of time. During SSA/ISSA imaging, however, the stacking is performed for each gridpoint inside the assumed velocity model at each time step. Therefore, the brightness function is always a function of both time (which corresponds to the assumed origin time) and space (which corresponds to the assumed hypocentre).

The other difference is that SSA/ISSA includes a number of data-processing steps before the waveforms/envelopes are used in the calculation of the brightness function. These steps, such as the amplitude normalization for individual stations and the weighting adjustment to account for the significantly different S/N conditions at different stations, are not necessary in the traditional DSM because most receivers are densely spaced. They are critical to the success of the SSA/ISSA because of the generally much larger interstation distance.

After the publication of the original SSA paper (Kao & Shan 2004), a series of similar DSM-based methods have been proposed in the literature to delineate the characteristics of seismic sources without performing phase picking (e.g. Baker *et al.* 2005; Ishii *et al.* 2005; Gajewski *et al.* 2007; Kao & Shan 2007; Rentsch *et al.* 2007; Anikiev *et al.* 2009; Kan *et al.* 2010; Zhebel *et al.* 2010; Kao *et al.* 2012). In fact, locating seismic sources without phase picking has been a focus of research since the early 1980s when seismological

research entered the digital era with increasingly powerful computation, communication and storage capabilities (e.g. McMechan 1982; McMechan *et al.* 1985; Rietbrock & Scherbaum 1994). As the amount of seismic data continues to increase worldwide, the ability to process huge acquisitions with minimal human intervention or interaction is quickly becoming a necessity for observational seismology.

Finally, a key advantage of these methods is that they can detect very weak events under extremely noisy conditions. This merit is especially important for aftershock studies that often involve a large data set containing numerous seismic events of all different sizes.

5.2 ISSA versus TR migration

A different approach to locate seismic sources without phase picking is the application of a TR process to 'rebroadcast' the observed seismic signals back to its source (e.g. McMechan 1982; Chang & McMechan 1991; Rietbrock & Scherbaum 1994; Fink 1997, 2006; Gajewski & Tessmer 2005; Larmat *et al.* 2006, 2008, 2010; Anderson *et al.* 2008). The numerical implementation of this 're-broadcasting' involves the construction of a full waveform field propagating through the media, meaning that not only *P* and/or *S* but all other phases are used in the relocation. It also eliminates the need to 'scan' specific model space for the existence of source(s) because the TR method only requires one simulation to 'bring back' all phases onto the source location at the right time. The obvious disadvantages are: (1) the computation is very intensive even with today's powerful computers, and (2) the choice of a velocity model that can correctly predict the arrivals of all phases becomes critical.

Essentially both ISSA and TR methods are based on the theorem of reciprocity. The SSA/ISSA makes use of this theorem in the form of establishing traveltime tables from every receiver position to all gridpoints in a 3-D model. It is evident that the advantages and disadvantages of TR are exactly the opposite for the ISSA. Theoretically, the ISSA can be considered as a much simplified version of TR that depends on only two phases (i.e. *P* and *S*). In fact, this is true for all 'back-projection' methods based on the DSM concept because the observed waveforms are migrated backwards according to the propagation speeds of one or two particular phases. To be more precise, TR propagates full waveforms backward in time until they finally constructively interfere at the source location, whereas the ISSA only uses the amplitude information to confirm the presents or absence of a seismic source at a certain time and location. This simplification enables the ISSA (and all other similar 'back-projection' methods for that matter) to take advantage of pre-calculated traveltime tables for fast calculation of the brightness function, thus making it an ideal source-location tool when computation time and/or cost are of concern.

5.3 Propagation and source radiation effects

A major advantage of ISSA is that the brightness calculation of each time-location pair is entirely driven by data. There is absolutely no need to separate the source term from the propagation effects during the brightness calculation. In fact, the brightness function is designed as the quantitative indicator for the likelihood of having a seismic source at a given time and location. Theoretically, a correction term for the effect of geometric spreading can be added to eqs 1 and 2 to preserve the absolute amplitude information. However, it does not add any significant benefit for our purpose but the extra computation can be overwhelming. This is especially true if the scanning is performed over the entire time and space domains. Instead, we deal with the geometrical spreading effect by normalizing individual waveform envelopes such that stations closer to the epicentre will not dominate the calculation of brightness.

Similarly, the brightness calculation is independent of the source radiation pattern. Although the observed amplitude is definitely influenced by the radiation pattern, the unlikely situation of all stations having near-zero amplitude can be easily avoided if the station coverage is adequate for the scanned model. Generally speaking, such an effect is insignificant if the largest azimuthal gap is less than 180° (Kao & Shan 2007; Kao *et al.* 2008; Kan *et al.* 2010).

5.4 Limitation and uncertainties of ISSA

Although the ISSA determines the spatiotemporal distribution of seismic sources from the amplitude information embedded in observed waveforms, the brightness function does not have a simple relationship with respect to the magnitudes of individual events. This is because the input waveform envelopes are normalized individually before they are used in the brightness calculation (eq. 2). Because the amplitude decreases with increasing epicentral distance, it is entirely possible for different sources to have significantly different (relative) amplitudes at the same station even if their sizes are more or less the same. For example, the assumed three sources in our synthetic experiments all have the same magnitude, but the corresponding amplitudes at each station vary significantly depending on the epicentral distances and source depths (Fig. 1). This is particularly obvious for stations located very close to one of the seismic sources such that their normalized waveforms would be dominated by the closest event. The resultant amplitude variation would consequently lead to different maximum brightness values, as demonstrated in Fig. 2. For this reason, it is important to include not only the largest brightness peak but also the minor peaks in the immediate vicinity if a complex, multiple-event scenario is expected.

The advantage of including additional phases in the ISSA analysis is twofold: (1) it can successfully suppress the artefacts caused by path and/or propagation effects (Figs 2b and c), and (2) it helps identify and eliminate spurious phases unrelated to the source events of interest. It does not necessarily imply, however, smaller hypocentral uncertainties. In fact, because the physical meaning of the brightness function of a seismic source (i.e. eq. 2) is fundamentally different from the physical meaning of the hypocentral uncertainty, the relationship between the two quantities is not straightforward. This point has been discussed in previous SSA papers (e.g. Kao & Shan 2004, 2007) and will not be repeated here. Generally speaking, factors that may broaden the brightness image, such as imperfect velocity models, poor signal-to-noise ratios, insufficient station coverage, and coarse scanning intervals, would also result in a larger hypocentral uncertainty. Although a detailed investigation on the effect of each aforementioned factor is important, it falls beyond the scope of this study. Our intention is to carry out such studies in the near future with carefully designed synthetic experiments. Using local earthquakes in the Cascadia subduction zone as calibration events, it has been documented that the 85 per cent contour of the peak normalized brightness value is a good proxy to the corresponding hypocentral uncertainty (Kao & Shan 2004; Kao *et al.* 2006). In this study, such an empirical approach appears acceptable.

We acknowledge that it is possible to design a more sophisticated way for the estimate of hypocentral uncertainties from an ISSA image. Specifically, if we follow the procedures proposed by

Witten & Artman (2011) to obtain the corresponding S/N distribution of the brightness image, the hypocentral uncertainties can be set according to a certain S/N threshold. The biggest advantage of this quantitative approach is that it has a statistical basis rather than being totally empirical. Moreover, it can automatically minimize the focusing/defocusing effects caused by complex velocity structures and eliminate the bias/artefacts because of uneven station distribution (Witten & Artman 2011). Implementation of a statistical procedure to estimate the uncertainties of ISSA solutions is planned in the near future.

5.5 Complementary role to phase-picking-based methods

Instead of advocating ISSA as a replacement, we emphasize the alternative role of the ISSA as a complement to conventional phase-picking methods, especially when highly accurate hypocentral locations of aftershocks or earthquake clusters are desired. In this case, the ISSA analysis could be used in the preliminary data screening stage to eliminate waveform records that are contaminated by local noise (thus enhance the data quality), as well as a robust reference to pinpoint the time windows so that accurate phase-picking data can be obtained with confidence. Such derived phase-picking files are essential to the success of conventional relocation methods, for example, the double difference method (Waldhauser & Ellsworth 2000) or the maximum intersection method (Font *et al.* 2004), in which the hypocentral mislocation because of imperfect velocity models can be greatly reduced. Therefore, it becomes possible to investigate comprehensively the complex aftershock distributions even for the time period immediately after a big main shock when the seismicity rate is the highest.

6 CONCLUSION

Earthquake aftershocks often occur closely in time and space. The large number of events can create a very difficult situation for conventional phase-picking process because seismic waveforms of different aftershocks might arrive at the same stations with little or no time difference. Conventional phase-picking process might also suffer the disadvantages of being time consuming, labour intensive, and having inconsistent quality if it is done by a group of analysts.

By systematically calculating the brightness function of all time-location pairs, the SSA can determine the time and location of a seismic source without the necessity of phase picking. In this study, we present an improved version of the SSA (ISSA) that is especially tuned for locating aftershocks or earthquake clusters. Specific improvements include the automatic determination of the window width used in the calculation of brightness function based on the spatial and temporal resolutions of the scanning process, a new weighting scheme to compensate the effects because of varying signal-to-noise ratios among stations, the application a ground motion analyser to separate the input waveforms into individual *P* and *S* traces, and a modified brightness function formula to combine constraints from both *P* and *S* phases.

A series of synthetic experiments that mimic an extremely complex scenario of aftershocks are conducted to demonstrate the advantages of the ISSA. We arrange the source-station geometry such that the arrivals of seismic phases at some stations are out of sequence. Conventional phase-picking methods fail in this difficult situation because the orders of arrivals from different events are no longer the same for all stations. Even the number of events cannot be confidently determined. The ISSA, in contrast, successfully recover the origin times and hypocentres of all input sources. Not only the number of events can be objectively determined from the number of distinctive peaks in the brightness function, but also the ambiguity of associating the same phase on different seismograms is completely avoided.

We apply the ISSA to a field data set selected from the OBS records of an offshore aftershock sequence southwest of Taiwan. Working with OBS data is especially challenging because of the relatively noisy environment and possible instrument disorientation. Despite of the extra complication, our ISSA analysis clearly delineates two events that can best explain the observed waveform pattern.

It is not our intention to promote the ISSA as a total replacement for traditional locating methods when the spatiotemporal distribution of seismic events can otherwise be properly resolved. Instead, we focus on more challenging scenarios when most phase-picking methods are expected to fail. The ISSA analysis can also be used as a complementary tool to improve the quality of phase picking when highly accurate hypocentral locations of aftershocks or earthquake clusters are desired.

ACKNOWLEDGMENTS

We are grateful to two anonymous reviewers for their constructive comments and to Alison Bird for proofreading the manuscript. Seismic Analysis Code (SAC) was used in data processing. Figures were generated using the Generic Mapping Tool (GMT) software (Wessel & Smith 1998). This manuscript was finished during a visit to the Pacific Geoscience Center, Geological Survey of Canada (GSC) by one of the authors (Y.-C. Liao) under the financial support of the National Science Council of Taiwan (NSC98–2917-I-008–106). Geological Survey of Canada ESS contribution 20110419.

REFERENCES

Anderson, B.E., Griffa, M., Larmat, C., Ulrich, T.J. & Johnson, P.A., 2008. Time reversal, *Acoust. Today,* **4**(1), 5–15.

Anikiev, D.V., Gajewski, D.J., Kashtan, B.M., Tessmer, E. & Vanelle, C., 2009. Localization of low-frequency microtremors by a modified diffraction stack, *71st EAGE Conf. Exhib.,* S040, http://www.earthdoc.org/detail.php?pubid=23983.

Audebert, F., Nichols, D., Rekdal, T., Biondi, B., Lumley, D.E. & Urdaneta, H., 1997. Imaging complex geologic structure with single-arrival Kirchhoff prestack depth migration, *Geophysics,* **62,** 1533–1543.

Baker, T., Granat, R. & Clayton, R.W., 2005. Real-time earthquake location using Kirchhoff reconstruction, *Bull. seism. Soc. Am.,* **95,** 699–707.

Bevc, D., 1997. Imaging complex structures with semirecursive Kirchhoff migration, *Geophysics,* **62,** 577–588.

Chang, W.-F. & McMechan, G.A., 1991. Wavefield extrapolation of body waves for 3-D imaging of earthquake sources, *Geophys. J. Int.,* **106,** 85–98.

Douglas, A., 1967. Joint epicentre determination, *Nature,* **215,** 47–48.

Du, W.-X., Thurber, C.H. & Eberhart-Phillips, D., 2004. Earthquake relocation using cross-correlation time delay estimates verified with the bispectrum method, *Bull. seism. Soc. Am.,* **94,** 856–866, doi:10.1785/0120030084.

Engdahl, E.R., 2006. Application of an improved algorithm to high precision relocation of ISC test events, *Phys. Earth Planet. Inter.,* **158,** 14–18.

Fink, M., 1997. Time reversed acoustics, *Phys. Today,* **50**(3), 34–40.

Fink, M., 2006. Time-reversal acoustics in complex environments, *Geophysics,* **71**(4), 1151–1164, doi:10.1190/1.2215356.

Font, Y., Kao, H., Lallemand S., Liu, C.-S. & Chiao, L.-Y., 2004. Hypocentre determination offshore of eastern Taiwan using the Maximum Intersection method, *Geophys. J. Int.,* **158,** 655–675.

Gajewski, D. & Tessmer, E., 2005. Reverse modelling for seismic event characterization, *Geophys. J. Int.,* **163,** 276–284.

Gajewski, D., Anikiev, D., Kashtan, B., Tessmer, E. & Vanelle, C., 2007. Localization of seismic events by diffraction stacking, *SEG Exp. Abstr.,* **26,** 1287–1291.

Gray, S.H. & May, W.P., 1993. Kirchhoff migration using eikonal equation traveltimes, *Geophysics,* **59,** 810–817.

Hole, J.A. & Zelt, B.C., 1995. 3-D finite-difference reflection traveltimes, *Geophys. J. Int.,* **121,** 427–434.

Ingate, S.F., Husebye, E.S. & Christoffersson, A., 1985. Regional arrays and optimum data processing schemes, *Bull. seism. Soc. Am.,* **75,** 1155–1177.

Ishii, M., Shearer, P.M., Houston, H. & Vidale, J.E., 2005. Extent, duration and speed of the 2004 Sumatra−Andaman earthquake imaged by the Hi-Net array, *Nature,* **435,** 933–936.

Kan, C.-W., Kao, H., Ou, G.-B., Chen, R.-Y. & Chang, C.-H., 2010. Delineating the rupture planes of an earthquake doublet using Source-Scanning Algorithm: application to the 3 March 2005 Ilan doublet, northeast Taiwan, *Geophys. J. Int.,* **182,** 956–966.

Kao, H. & Shan, S.-J., 2004. The Source-Scanning Algorithm: mapping the distribution of seismic sources in time and space, *Geophys. J. Int.,* **157,** 589–594.

Kao, H. & Shan, S.-J., 2007. Rapid identification of earthquake rupture plane using Source-Scanning Algorithm, *Geophys. J. Int.,* **168,** 1011–1020.

Kao, H., Shan, S.-J., Dragert, H., Rogers, G., Cassidy, J.F., Wang, K., James, T. & Ramachandran, K., 2006. Spatial-temporal patterns of seismic tremors in northern Cascadia, *J. geophys. Res.,* **111,** B03309, doi:10.1029/2005JB003727.

Kao, H., Wang, K., Chen, R.-Y., Wada, I., He, J. & Malone, S.D., 2008. Identifying the rupture plane of the 2001 Nisqually, Washington, earthquake, *Bull. seism. Soc. Am.,* **98,** 1546–1558.

Kao, H. *et al*., 2012. Locating, monitoring, and characterizing typhoon-induced landslides with real-time seismic signals, *Landslides,* doi:10.1007/s10346-012-0322-z.

Klein, F.W., 1978. Hypocenter location program HYPOINVERSE, Open-File Rep, U.S. Geol. Surv. 78–694, 113pp.

Larmat, C., Montager, J.P., Fink, M., Capdeville, Y., Tourin, A. & Clevede, E., 2006. Time-reversal imaging of seismic sources and application to the great Sumatra earthquake, *Geophys. Res. Lett.,* **33,** L19312, doi:10.1029/2006GL026336.

Larmat, C., Tromp, J., Liu, Q. & Montagner, J.P., 2008. Time reversal location of glacial earthquakes, *J. geophys. Res.,* **113,** B09314, doi:10.1029/2008JB005607.

Larmat, C., Guyer, R. & Johnson, P., 2010. Time-reversal methods in geophysics, *Phys. Today,* **63**(8), 31–35.

Lee, W.H.K. & Lahr, J.C., 1975. HYPO71 (Revised): a computer program for determining hypocenter, magnitude, and first motion pattern of local earthquakes, Open-File Rep, U.S. Geol. Surv. 75–311, 113pp.

Liao, Y.-C., Hsu, S.-K., Chang, C.-H., Doo, W.-B., Ho, M.-Y., Lo, C.-L. & Lee, C.-S., 2008. Seismic tomography off SW Taiwan: a joint inversion from OBS and on shore data of 2006 Pingtung aftershocks, *Terr. Atmos. Ocean. Sci.,* **19,** 729–741, doi:10.3319/TAO.2008.19.6.729(PT).

Mao, W. & Gubbins, D., 1995. Simultaneous determination of time delays and stacking weights in seismic array beamforming, *Geophysics,* **70,** 491–502.

McIntosh, K., Nakamura, Y., Wang, T.-K., Shih, R.-C., Chen, A. & Liu, C.-S., 2005. Crustal-scale seismic profiles across Taiwan and the western Philippine Sea, *Tectonophysics,* **40,** 23–54, doi:10.1016/j.tecto.2005.1002.1015.

McMechan, G.A., 1982. Determination of source parameters by wavefield extrapolation, *Geophys. J. Int.,* **71,** 613–628.

McMechan, G.A., Luetgert, J.H. & Mooney, W.D., 1985. Imaging of earthquake sources in Long Valley Caldera, California, 1983, *Bull. seism. Soc. Am.,* **75,** 1005–1020.

Rentsch, S., Buske, S., Luth, S. & Shapiro, S.A., 2007. Fast location of seismicity: a migration-type approach with application to hydraulic-fracturing data, *Geophysics,* **72,** S33–S40, doi:10.1190/1.2401139.

Rietbrock, A. & Scherbaum, F., 1994. Acoustic imaging of earthquake sources from the Chalfant Valley, 1986, aftershock series, *Geophys. J. Int.,* **119,** 260–268.

Rosenberger, A., 2010. Real-time ground motion analysis: distinguishing *P*- and *S*-arrivals in a noisy environment, *Bull. seism. Soc. Am.,* **100**(3), 1252–1262, doi:10.1785/0120090265.

Thurber, C.H., 2011. Earthquake, location techniques, in *Encyclopedia of Solid Earth Geophysics,* pp. 201–206, ed. Gupta, H.K., Springer, Dordrecht, the Netherlands.

Waldhauser, F. & Ellsworth, W.L., 2000. A double-difference earthquake location Algorithm: method and application to the northern Hayward fault, California, *Bull. seism. Soc. Am.,* **90**(6), 1353–1368, doi:10.1785/0120000006.

Wessel, P. & Smith, W.M.F., 1998. New improved version of generic mapping tools released, *EOS, Trans. Am. Geophys. Union,* **79,** 579, doi:10.1029/98EO00426.

Witten, B. & Artman, B., 2011. Signal-to-noise estimates of time-reverse images, *Geophysics,* **76,** MA1–MA10.

Zhebel, O., Gajewski, D. & Vanelle, C., 2010. Localization of seismic events in 3D media by diffraction stacking, *SEG Exp. Abstr.,* **29,** 2181–2185.

Zhou, H.-W., 1994. Rapid three-dimensional hypocentral determination using a master station method, *J. geophys. Res.,* **99,** 15 439–15 455.

Zhu, L. & Rivera, L.A., 2002. A note on the dynamic and static displacements from a point source in multilayered media, *Geophys. J. Int.,* **148,** 619–627.